

## RESEARCH ARTICLE

# Monitoring of fused filament fabrication (FFF): An infrared imaging and machine learning approach

Niklas Bauriedel<sup>1</sup> | Rodrigo Q. Albuquerque<sup>1</sup> | Julia Utz<sup>1</sup> | Nico Geis<sup>2</sup> |  
Holger Ruckdäschel<sup>1,2</sup> 

<sup>1</sup>Department of Polymer Engineering,  
University of Bayreuth, Bayreuth,  
Germany

<sup>2</sup>Division Polymers, Neue Materialien  
Bayreuth GmbH, Bayreuth, Germany

**Correspondence**

Holger Ruckdäschel, University of  
Bayreuth, Universitätsstrasse 30, Bayreuth  
95447, Germany.

Email: [holger.ruckdaeschel@uni-bayreuth.de](mailto:holger.ruckdaeschel@uni-bayreuth.de)

**Abstract**

Additive manufacturing holds great promise for broader future use, but quality assurance and component monitoring present notable challenges. This study tackles monitoring Fused Filament Fabrication (FFF) via infrared imaging to forecast the mechanical traits of 3D-printed items. It highlights how temperature variations, influenced by the infill's alternating orientation, affect printed parts' mechanical properties. Utilizing Machine Learning, notably the Random Forest Regressor, this research validates the capability to accurately predict tensile strength from infrared temperature readings, offering a simple, yet effective, real-time FFF monitoring method without specialized hardware. This approach enhances the quality and dependability of 3D-printed components with IR thermal monitoring and machine learning predictions.

**Highlights**

- Infrared imaging and machine learning are combined to monitor 3D printing.
- A cost-effective and accessible non-destructive monitoring method is proposed.
- Temperature variation patterns of 3D printed layers influence mechanical properties.

**KEYWORDS**

additive manufacturing, fused filament fabrication, IR imaging, machine learning, mechanical properties

## 1 | INTRODUCTION

Additive Manufacturing (AM) offers numerous advantages, making it a promising technology for various applications. One of its common applications is Rapid Prototyping, enhancing development processes by facilitating the fabrication of parts in numerous geometries with ease, speed, and

cost-effectiveness. Additionally, AM is utilized to integrate personalized components into end-user products, thereby minimizing material waste and enhancing sustainability.<sup>1</sup>

There exist several techniques for AM, including Selective Laser Sintering (SLS), Digital Light Processing (DLP), Laminate Object Manufacturing (LOM), Fused Filament Fabrication (FFF), and others, allowing for a

This is an open access article under the terms of the [Creative Commons Attribution](https://creativecommons.org/licenses/by/4.0/) License, which permits use, distribution and reproduction in any medium, provided the original work is properly cited.

© 2024 The Author(s). *Journal of Polymer Science* published by Wiley Periodicals LLC.

wide variety of materials to be used, such as thermoplastic polymers, thermoset polymers, metals, or ceramics. Each method presents its own set of advantages and disadvantages, suitable for different applications.<sup>2</sup>

However, obstacles hindering its adoption beyond prototyping include lack of expertise, limited material choices, and integration challenges within existing manufacturing processes such as the conversion of existing production lines. Concerns about component quality and the absence of suitable options for inline quality monitoring also pose significant challenges.<sup>3,4</sup>

Cost is another major consideration when contemplating the adoption of AM. Although traditional manufacturing methods often exhibit cost advantages, AM can offer benefits for specific use cases. Entry costs, including equipment purchase, integration into existing processes, and employee training, constitute a substantial initial investment. Additionally, ongoing costs such as materials, energy, and working time should be taken into account. While initial costs are typically fixed, running costs present opportunities for optimization. Due to the time-intensive nature of the AM process, early defect monitoring offers the opportunity to detect process errors at an early stage and thus save costs due to less wasted goods and time savings.

Early identification of potential problems in the manufactured part allows for process interruption or adjustment, thereby avoiding unnecessary costs. Moreover, data generated during the printing process can provide further insights into the finished object.<sup>4,5</sup>

Fused Filament Fabrication is often preferred for polymer materials due to its simplicity, cost-effectiveness, and versatility in handling a wide range of thermoplastic polymers.<sup>6</sup> However, temperature management is crucial in FFF, as incorrect temperatures can lead to various issues, such as warping, shrinkage, nozzle clogging, or choking.<sup>7</sup>

Another critical aspect is the adhesion between individual layers and within a layer, which is strongly influenced by temperature. Inadequate temperature control may result in reduced adhesion and poor mechanical properties of the finished part.<sup>8</sup>

Oleff et al.<sup>9</sup> reviewed monitoring techniques applicable to FFF, categorizing them into six distinct groups: 2D-vision, temperature monitoring, vibration monitoring, 3D-vision, acoustic emission monitoring, and electrical quantity monitoring.

Monitoring methods can be categorized into monitoring the components of the printer or monitoring the printed part directly. A 3D printer comprises numerous components, each serving specific functions and offering various parameters that can be monitored. Malfunction in any component can lead to quality issues in the finished part. Options for monitoring include listening to acoustic signals to detect filament breakage,<sup>10</sup> analyzing

vibrations to detect printer errors,<sup>11</sup> or using sensors built into the printer for monitoring flow rates in the nozzle,<sup>12</sup> among others.

Direct monitoring of components can be categorized based on the viewpoint obtained, such as top view, side view, or accumulated information about the entire component. This information can be used to ensure that the printed part maintains its intended shape<sup>13</sup> or to plan post-processing procedures like milling.<sup>14</sup>

Despite the availability of various monitoring methods, they often come with significant drawbacks, such as being time-consuming to set up and integrate, requiring specialized and costly hardware, and their inability to provide definitive statements about the final printed parts.

This work aims to provide a simple and cost-effective solution to monitor and control FFF-based 3D printing processes using infrared (IR) images, and to predict the mechanical properties of the final printed part using the recorded IR information.

The following approach is implemented: monitoring the temperature of the newly extruded material and thus the temperature of each printed layer. The setup should be simple, affordable, and should not require specialized hardware, such as dedicated printers or excessively small IR cameras. A Machine Learning (ML) model is trained to predict mechanical properties, namely the tensile strength, from the measured temperatures of all layers of a given printed part.

## 2 | MATERIALS AND METHODOLOGY

### 2.1 | Printer

For this study, a Raise3D Pro 2 printer (Raise3D Technologies, Inc., CA) was used. It offers sufficient space for positioning the IR-camera. Nozzles with a diameter of 0.4 mm are used. Slicing was done with the software ideaMaker from Raise3D. Further details on the printing process can be found in subsection 2.3.

### 2.2 | Filament

Various thermoplastic polymers can be used for the FFF, such as ABS, PP, PET, and others. One of the most commonly used materials for the FFF is polylactide acid (PLA).<sup>15</sup>

Polylactide acid was also used in this work. With this choice of material, the work closely resembled common printing tasks, as would be expected in an environment where a simple and cost-effective way of monitoring is

required. Another advantage of using PLA is the wide temperature range in which it can be processed. The PLA filament used in this work was a commercially available BASF Ultrafuse PLA GREEN filament (BASF printing solutions GmbH, Heidelberg, Germany), with a diameter of 1.75 mm.

### 2.3 | Printed tensile bars and printing parameters

A quality characteristic for parts manufactured with FFF is the adhesion between the individual layers. A way to analyze layer adhesion is performing a tensile test on a tensile part printed in a standing upright position.<sup>16</sup>

As test objects, tensile bars with a larger geometry were chosen. To obtain a sufficient number of temperature values through the IR-measurements, the layers must be of an appropriate size. For this reason, the geometry of the tensile bars was selected as shown in Figure 1. In order to have consistently sized IR-images for each layer, with the full part visible, only the images of the gray marked area (from layer #70 to layer #160) of the tensile bars were used later on. This area also corresponds to the section where the tensile bar is most likely to break. For standardized tensile test (According to DIN ISO 527), the bars have to break in this area to be valid. The tensile testing was carried out on the universal

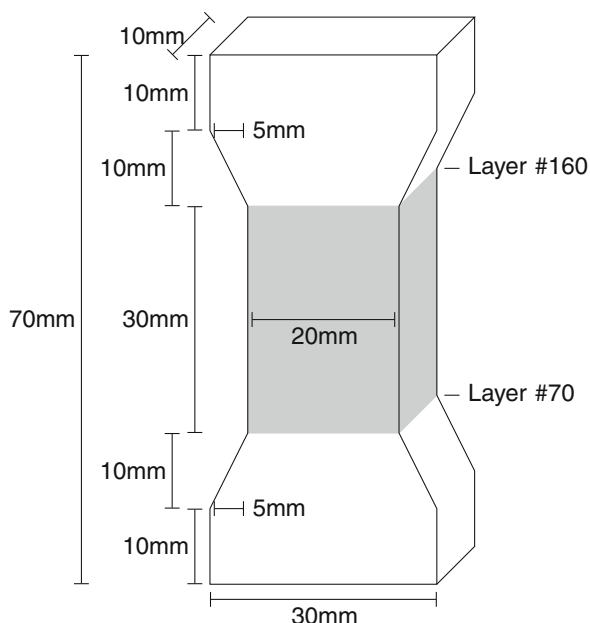


**FIGURE 1** Geometry of the tensile bars used. The tensile bars are larger and more massive than standardized ones. The aim was to provide a higher surface or cross-section area and, with that, more temperature values per layer.

testing machine Zwick Z020 (ZwickRoell GmbH & Co KG, Ulm, Germany) with a testing speed of 50 mm/min.

To generate input data with variations in tensile strength through material temperature, two parameters were varied. The first parameter was the nozzle temperature. The recommended nozzle temperature for the used PLA is 210 °C, but both higher and lower temperatures are also feasible for printing with this material. The mechanical properties of AM manufactured parts can be influenced by various processing parameters.<sup>17</sup> A direct influence can be achieved by parameters that directly influence the melting behavior. The nozzle temperature naturally has a direct influence on the temperature of the melt and, thus, on the welding quality and the tensile strength.

A more indirect way to influence the melting behavior and with that the temperature of the melt is by varying the material of the nozzle. Brass is normally used for materials, such as PLA, due to its good thermal conductivity. Steel nozzles, which have a poorer thermal conductivity, are sometimes used for more abrasive materials. Using a steel nozzle with PLA should also affect the material temperature.<sup>18</sup>

Nozzle temperatures of 180, 190, 210, and 230 °C were used in combination with a brass nozzle, and 200 and 220 °C with a steel nozzle. Temperatures outside this range led to problems with printing or the generation of IR-images.

Five tensile bars were printed for each of the six nozzle temperature and nozzle material combinations, resulting in  $5 \times 6 = 30$  possible data points. However, the tensile test for two tensile bars (One with 210 and one with 200) failed and did not deliver usable data, leaving a total of 28 data points.

Four bars encountered issues during the tensile testing. These issues might justify excluding these four bars from the machine learning dataset, leaving 24 bars. Further details about this incident are provided in subsection 3.2.

Another important factor during printing is ensuring that the layers are thick enough so that transmission of heat radiation through one layer can be neglected in the IR-measurements. A layer thickness of 0.3 mm was used. The infill density must be 100% to achieve a closed area with valid temperature values. Other parameters can be found in Table 1 and are common for processing this PLA grade.

### 2.4 | Infrared measurement

The IR-camera used in this work is the Optris Xi 400 (Optris GmbH, Berlin, Germany), which is compact in size and can easily be positioned on the 3D printer. It has a resolution of  $382 \times 288$  pixels and is capable of measuring temperatures in three different ranges.

**TABLE 1** Process parameters used for all printed tensile bars. Varied parameters were the nozzle temperature and the nozzle material.

Parameter	Value
Nozzle temperature	180 – 230 °C
Nozzle material	brass/steel
Heatbed temperature	60 °C
Layer height	0.3 mm
Infill density	100%
Infill pattern	Grid
Default printing speed	50 mm/s
Infill printing speed	50 mm/s

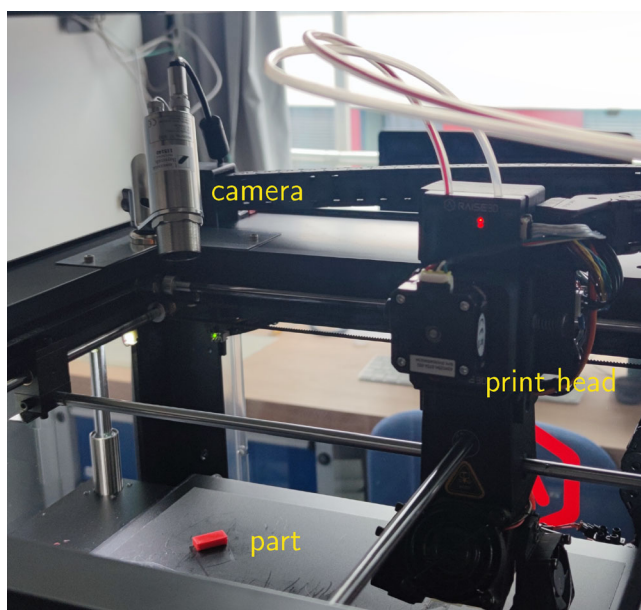


**FIGURE 2** Attachment of the camera to the printer to image the parts printed in the respective corner.

For this work, a temperature range of 0–250 °C was utilized. Additionally, it represents a cost-effective option among IR-cameras.

The camera was strategically positioned to overlook the currently printed part, enabling it to capture images as soon as the print head moved out of the field of view. The setup is illustrated in Figure 2. The printing process was conducted as close to the corner of the camera's view as possible, while ensuring that there was no risk of interference from parts of the printer. The objective was to capture images at an acute angle.

Following the work by Morgan et al.,<sup>19</sup> the emissivity value for the IR-measurement was set to 0.92. The layer height was chosen to be high enough so that transmission could be neglected (see subsection 2.3).

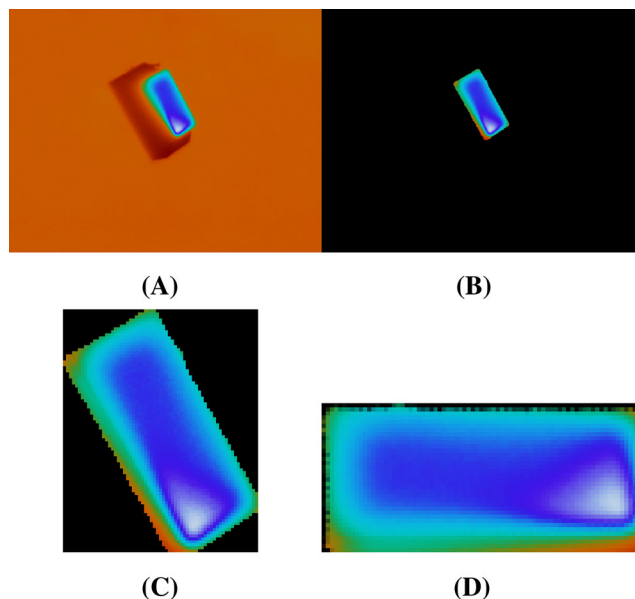


**FIGURE 3** Visualization of the different pre-processing steps for the IR-images. (A) Directly captured image without pre-processing. (B) Unnecessary pixels/temperatures are set to black/0 °C. (C) Cropping of the image around a bounding-box. (D) Cropping of the image around a minimal rotated rectangle.

## 2.5 | Generating infrared measurements for each layer

During the printing process, one IR-image per layer was captured. The printer was programmed so that after printing each layer, the print head moves out of the way. With the head moved aside, the part becomes completely visible to the IR-camera. The camera captures one image per second. The images are classified by a simple ML model into images with the printing head (*Bad*) and images without the printing head (*Good*). As soon as a *Good* image is recognized, it is stored, and the camera is paused for a few seconds to wait for the printer to start the next layer.

After taking a snapshot (Figure 3A), it is noted that many areas in the images do not belong to the actual object or are part of the sidewall. Including these pixels in the final dataset could affect the results, thus necessitating their removal. For this purpose, a map is utilized to indicate which pixels (temperature values) belong to the object and which do not. This map is created in advance and applied to each image, resulting in an image where only the printed part is colored, and everything else is set to black (or to 0 °C) (Figure 3B). Unnecessary regions are also removed using a bounding-box (Figure 3C) or a minimal rotated rectangle (Figure 3D) around the printed part.

## 2.6 | Machine learning

With the data now generated, the model building to predict tensile strength can commence. Initially, the model should be relatively simple. Therefore, not all measured temperature values are used (there are about 2700 values per layer, and images of 90 layers are generated).

Instead, the minimum, maximum, and average temperatures of each layer and of the entire object are calculated. Additionally, the average of all maximum and minimum values per layer is computed.

In subsequent models, these five features are used: the minimum value over the entire object (Min Overall), the maximum value over the entire object (Max Overall), the average value over the entire object (Avg Overall), the average of the minimum values per layer (Avg Min), and the average of the maximum values per layer (Avg Max).

An alternative approach that was explored involved using the minimum, maximum, or average temperature value of each individual layer. However, this approach was more complex and did not yield better results, so it was discarded.

The dataset was divided into a training set and a test set, with 20% of the dataset allocated for testing. This means the training dataset contains 23 data points, and the test dataset contains 6. The feature values of the training dataset were scaled to unit variance. The same scaling was applied to the test dataset, and this scaling must also be applied to make predictions for new values. Only the training dataset was used to optimize the models. The test dataset was unseen by any model and was only used to compare the different ML models and to validate the model with unknown data.

Hyperparameter optimization was performed to refine a model. For this purpose, a  $k$ -fold cross-validation was conducted. The training dataset was divided into  $k$  different blocks, with the model trained on  $k - 1$  blocks and the omitted block used as the validation dataset. A  $k$  value of 4 was used, meaning three validation sets have 6 elements each, and one has only 5 elements. The Mean Absolute Error (MAE) (1) was used as the validation metric. The process continues until each block has been used once for validation. The average MAE across all folds is calculated.<sup>20</sup>

$$\text{MAE} = \frac{1}{n} \sum_{i=1}^n |y_i - \hat{y}_i| \quad (1)$$

$n$ : Number of observations  
 $y_i$ :  $i$ -th actual value  
 $\hat{y}_i$ :  $i$ -th predicted value

To compare different hyperparameters, the calculated average MAE is used. The hyperparameter set with the

lowest MAE is then used to train the model again with the entire training dataset. This process is repeated for every ML model experimented with. To compare the performance of the models, the MAE and the  $R^2$ -score (2) are used.

$$R^2 = 1 - \frac{\sum_{i=1}^n (y_i - \hat{y}_i)^2}{\sum_{i=1}^n (y_i - \bar{y})^2} \quad (2)$$

$n$ : Number of observations  
 $y_i$ :  $i$ -th actual value  
 $\hat{y}_i$ :  $i$ -th predicted value  
 $\bar{y}$ : Mean of the actual values

Experiments were conducted with the following ML models, all implemented with scikit-learn.<sup>21,22</sup>

*(Least Squares) Linear Regression (LR)* The LR model fits a linear function to the data without any hyperparameters for optimization. It serves well as a benchmark model due to its simplicity.<sup>23</sup>

*Multi-Layer Perceptron (MLP)* A MLP is a basic feed-forward neural network consisting of an input layer, several hidden layers, and an output layer. The neurons in these layers perform a weighted summation followed by an activation function. Parameters for optimization include the number of hidden layers, neurons per layer, activation function (logistic/Sigmoid or Rectified Linear unit (ReLU)), and the solver (L-BFGS, Stochastic Gradient Descent (SGD), or Adam).<sup>24</sup>

*Support Vector Regression (SVR)* The SVR aims to find a hyperplane in a higher-dimensional space to separate data points while minimizing prediction error. Optimized parameters include regularization (C) and the kernel type (linear, Radial Basis Function (RBF), or Sigmoid).<sup>25</sup>

*Random Forest Regression (RFR)* A RFR trains multiple decision trees on random subsets of the dataset, with the final prediction being an aggregation of all trees' predictions. Optimized parameters include the number of trees, performance measurement function (absolute error or Poisson), and the maximum depth of trees.<sup>26</sup>

*k-Nearest-Neighbor regression (kNN)* The kNN model predicts based on the  $k$  nearest neighbors in the training dataset. Parameters such as the number of neighbors, weight function, and distance calculation method are optimized.<sup>27</sup>

## 3 | RESULTS AND DISCUSSION

### 3.1 | Temperature values

Figure 4 shows a representative example of the minimum, maximum and average temperature for each layer. It is noticeable that a slightly higher temperature always

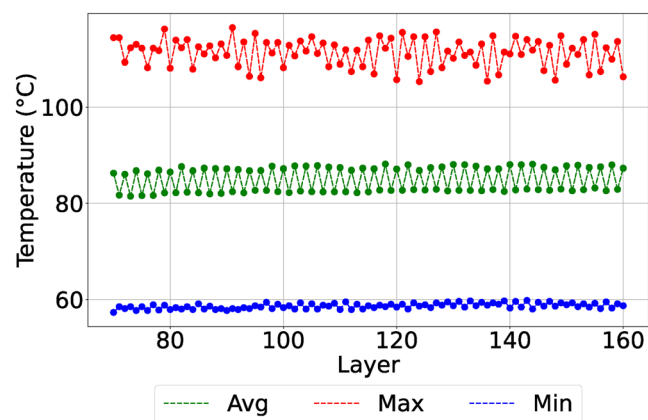


**FIGURE 4** Minimum (blue), maximum (red) and average (green) temperature value for each layer (nozzle temperature: 210 °C, nozzle material: Brass).

alternates with a slightly lower temperature, best seen on the average temperature values.

The reason for this is that not every layer is printed in the same way. The orientation of the infill pattern always alternates. This means that the print head is quicker out of the camera's view for even layers than it is for odd layers. As a result, the material has more time to cool down with odd-numbered layers, which can be measured by the IR-camera.

Fluctuations can be clearly seen in the maximum values, while the average values remain relatively stable. The minimum values do not show any major fluctuations. A reason is the heat flow. The closer the material temperature gets to the ambient temperature, the lower the influence of cooling time. This effect is visible in the fluctuations and can be intensified by imperfect cropping at the edges, which can lead to the visibility of previous layers.

### 3.2 | Tensile tests

The modified geometry, the increased size of the tensile bars in this study introduced several challenges during tensile testing. Contrary to expectations, not all bars fractured at the intended narrow midsection (Figure 5A). Frequently, fractures occurred near the junction of the narrow and wide sections of the bars (Figure 5C). This could either indicate an often occurring weakness of the printed structure or a stress concentration due to the simplified design of the tensile bar. Despite these irregularities, the tensile test results remain reliable and trustworthy. However, it is not always possible to confirm whether infrared (IR) images were captured at the exact fracture layer, though they are still applicable for model development.

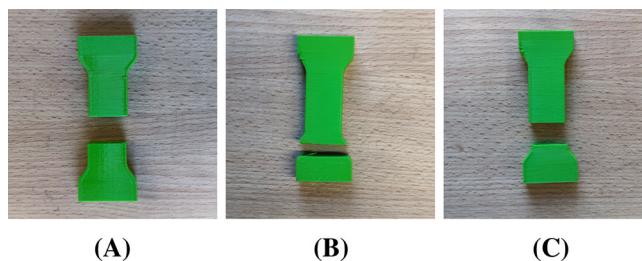


**FIGURE 5** Example for the tensile bars after the tensile tests. a Broken in the narrow area. b Broken near the clamping. c Broken near the transition.

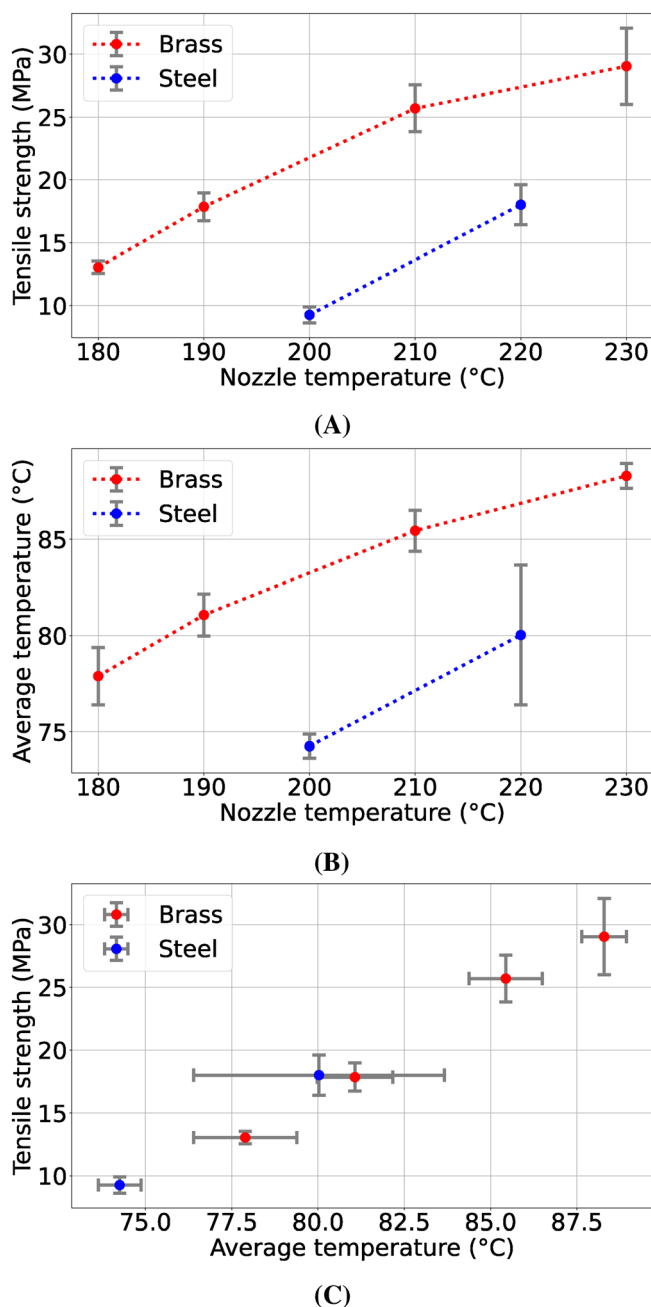
Additionally, some bars fractured at the broad section, close to the clamping (Figure 5B). Due to the relationship between the tensile strength and the cross-section area, this will invalidate the calculated tensile strength. In total four bars broke near the clamping (One with 200 and three with 180 °C). The analysis included models trained with all 28 bars and a subset excluding the four affected bars (24 bars). This study presents the models excluding these four bars. Although the performance metrics for both sets of models were comparable, detailed results incorporating the four bars are available in the [supplementary information](#).

In Figure 6, three diagrams show that the desired variation in temperatures and tensile strength can be achieved by changing the nozzle temperature and the nozzle material. Figure 6A shows that the tensile strength increases for one nozzle material with higher nozzle temperatures and that the tensile strength is lower for the steel nozzle than for the brass nozzle. This can be correlated with the temperatures measured with the IR-camera. In Figure 6B it can be seen that the measured temperature for the steel nozzle is lower and so the temperature of the extruded material is lower using a steel nozzle. In general, the measured material temperature of a nozzle material increases with the nozzle temperature. Figure 6C shows that the tensile strength increases with increasing material temperatures. One of the main reasons for this increase in tensile strength is the better adhesion and welding of the layers at higher material temperatures.

### 3.3 | Machine learning models

The model optimization using the training set delivered a set of hyperparameters for each model used. The optimized hyperparameters are as follows:

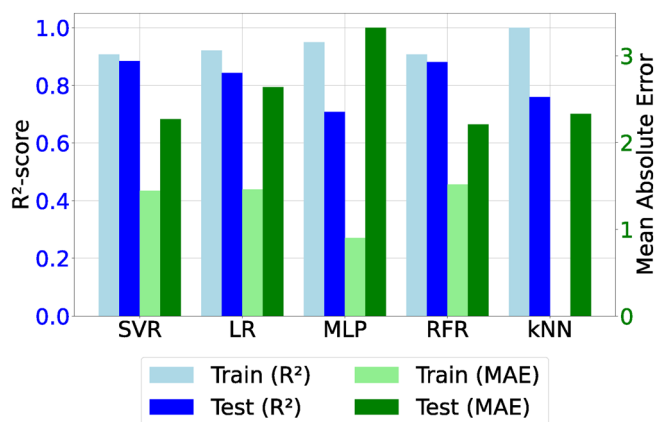
1. SVR:  $C$ -value of 10 coupled with a *linear* kernel.
2. MLP: *Logistic* activation function, Low-memory Broyden–Fletcher–Goldfarb–Shanno algorithm (L-BFGS)



**FIGURE 6** (A) Comparison of nozzle temperatures (x-axis) with the measured tensile strength (y-axis) for different nozzle materials (brass in red, steel in blue). (B) Comparison of nozzle temperatures (x-axis) with the measured material temperatures (y-axis) for different nozzle materials (brass in red, steel in blue). (C) Comparison of tensile strength with nozzle temperatures and the average measured material temperatures across the entire part.

as the solver, and a network architecture consisting of one hidden layers with two neurons.

3. RFR: *Poisson* as the measure, 50 decision trees and a maximum depth of two.
4. kNN: One nearest neighbors, employing uniform weight and utilizing the Minkowski distance of order three as the metric.



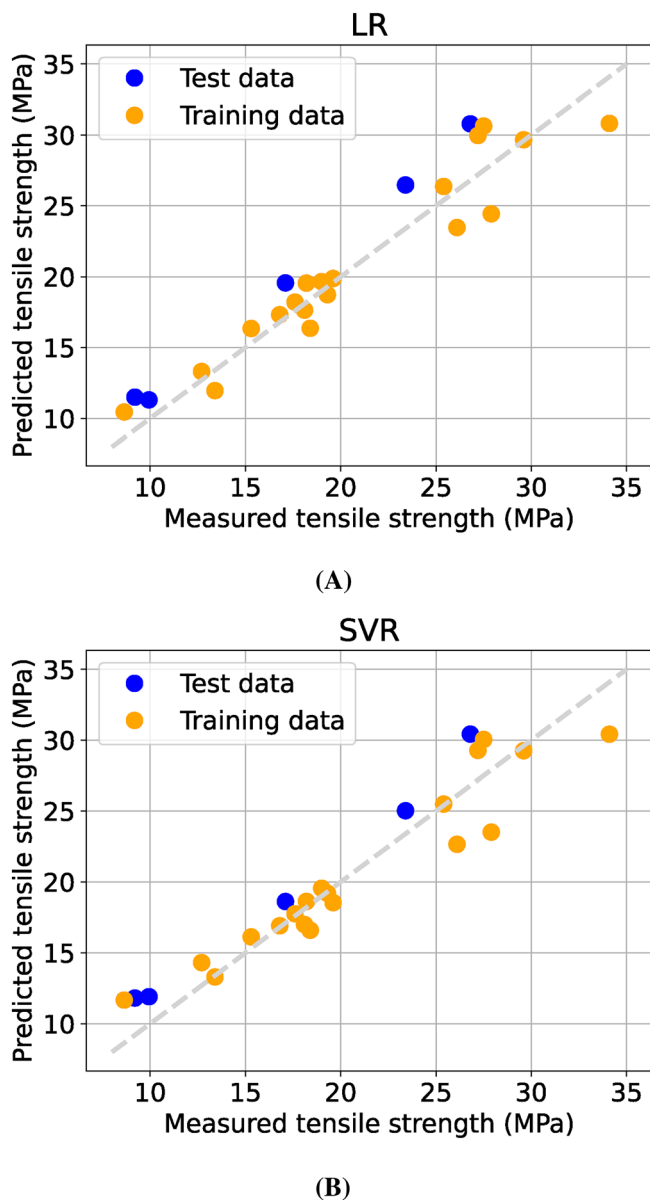
**FIGURE 7** Comparison of the  $R^2$ -score and the Mean Absolute Error (MAE) for the five optimized models. In each case for training and the test data set.

Figure 7 shows the  $R^2$ -Score and Mean Absolute Error (MAE) for the five models trained with the optimized hyperparameters on the training set. The metrics were calculated separately for the data points in the training and test sets.

The kNN exhibits significant overfitting, as evidenced by a MAE of zero on the training dataset and a high MAE on the test set. Also the MLP shows evidence of a slight overfitting. Both the  $R^2$ -score and the MAE show clear differences between training and test set. The other models performed well, even in the case of the simple LR, which was used as a reference. Support Vector Regression and RFR yielded good and similar results. Specifically, the SVR achieved an  $R^2$ -score of 0.88 and a MAE of 2.3 MPa on the test set, while on the training set, it scores 0.90 and 1.4 MPa. Comparably, the RFR achieves 0.87 and 2.2 MPa on the test set and 0.90 and 1.5 MPa on the training set, making its results highly comparable to those of the SVR.

The measured and predicted tensile strengths are in good agreement. In Figure 8, two examples are illustrated: the first with the LR serving as the reference model, and the second showcasing the SVR as one of the superior models. Although the predicted values from both models are close to the measured ones, it is evident that the predictions made with the SVR are more accurate. Again the results for the SVR and the RFR are comparable.

Despite the slight advantages of the SVR and the RFR discussed earlier, LR also offers several advantages. Linear Regression is highly interpretable, allowing easy understanding of the impact of each feature on the predictions after training. The absence of hyperparameters enables fast and easy model generation without the need for hyperparameter optimization. The training time of a



**FIGURE 8** Comparison of the predicted tensile strength with the measured tensile strength. (A) (Least Squares) Linear Regression (for reference). (B) Support Vector Regression.

LR model is typically also quite short. Linear Regression performs well even for small training data sets and minimizes the risk of overfitting. The advantages can also be seen in the predictions from Figure 8A, where a good accuracy was obtained.

## 4 | CONCLUSION

The models trained in this study have demonstrated their ability to make accurate predictions on unknown data (test set). However, there are limitations that should be addressed in future work. An obvious limitation is the

limited amount of training data available. This work was focused on only one PLA grade. To enhance the applicability of such models in general 3D printing processes, it would be beneficial to take into account varied geometries of the printed part.

The objective of monitoring the FFF process using infrared cameras and predicting the mechanical properties of the printed parts from IR pixels was successfully achieved.

This study demonstrates that accurate predictions can be made with a relatively simple setup and straightforward models. This finding suggests a viable path toward a simple, cost-effective, and accessible method for monitoring FFF processes, notably without the need for specialized printers or additional hardware. The methodology presented here can be adapted to any combination of printer and infrared camera.

Regression analysis was employed to predict the mechanical properties of the printed components. The models trained in this study have shown promising results, affirming the feasibility of this prediction approach.

Looking forward, a crucial step for enhancing this research would be to augment the dataset. Furthermore, the quality of data could be improved by optimizing the IR-images captured during the process. Exploring the use of alternative IR-cameras with higher resolutions or greater zoom capabilities could yield more detailed and nuanced temperature data per layer. Minimizing the influence of print head movement on the temperature readings may also refine the results. Additionally, adopting more sophisticated ML-models could potentially enhance prediction accuracy.

Moreover, enriching the model by incorporating data from various materials could make the predictions more robust and widely applicable.

In summary, this work establishes the viability of using infrared cameras to monitor the FFF process and demonstrates the potential of predicting mechanical properties based on the surface temperatures measured during printing.

## ACKNOWLEDGMENT

Open Access funding enabled and organized by Projekt DEAL.

## ORCID

Holger Ruckdäschel  <https://orcid.org/0000-0001-5985-2628>

## REFERENCES

- [1] M. Attaran, *Business Horiz.* **2017**, *60*, 677.
- [2] S. K. Parupelli, S. Desai, *Am. J. Appl. Sci.* **2019**, *16*, 244.
- [3] Hubs, *Additive Manufacturing Trend Report 2021*, Hubs, a Protolabs Company, Amsterdam **2021** <https://f.hubspotusercontent10.net/hubfs/4075618/Additive%20manufacturing%20rend%20report%202021.pdf>

- [4] L. Yi, C. Gläßner, J. C. Aurich, *J. Manuf. Syst.* **2019**, 53, 195.
- [5] N. Hopkinson, P. Dicknes, *Proc. Instit. Mech. Eng. C* **2003**, 217, 31.
- [6] M. Heidari-Rarani, M. Rafiee-Afarani, A. M. Zahedi, *Compos. B Eng.* **2019**, 175, 107 147.
- [7] A. Yadav, P. Rohru, A. Babbar, R. Kumar, N. Ranjan, J. S. Chohan, R. Kumar, M. Gupta, *Int. J. Interact. Des. Manuf.* **2022**, 17, 2867. <https://doi.org/10.1007/s12008-022-01026-5>
- [8] A. Lepoivre, N. Boyard, A. Levy, V. Sobotka, *Procedia Manuf.* **2020**, 47, 948.
- [9] A. Oleff, B. Küster, M. Stonis, L. Overmeyer, *Progress Addit. Manuf.* **2021**, 6, 705.
- [10] Z. Yang, L. Jin, Y. Yan, Y. Mei, *Sensors* **2018**, 18, 749.
- [11] J. Liao, Z. Shen, G. Xiong, C. Liu, C. Luo, J. Lu, *Conf. Ind. Electron. Appl.* **2019**, 6, 2098.
- [12] V. Klar, J. M. Pearce, P. Kärki, P. Kuosmanen, *HardwareX* **2019**, 6, e00080.
- [13] A. R. Fahmy, T. Becker, M. Jekle, *Innov. Food Sci. Emerg. Technol.* **2020**, 63, 102384.
- [14] F. Alhwarin, A. Ferrein, A. Gebhardt, S. Kallweit, I. Scholl, O. Tedjasukmana, *2015 IEEE International Conference on Automation Science and Engineering (CASE)*, IEEE, Sweden **2015**, p. 924. <https://doi.org/10.1109/CoASE.2015.7294217>
- [15] A. Dey, I. N. Roan Eagle, N. Yodo, *J. Manuf. Mater. Process.* **2021**, 5, 69.
- [16] A. Sola, W. J. Chong, D. Pejak Simunec, Y. Li, A. Trinchi, I. L. Kyratzis, C. Wen, *Polym. Test.* **2023**, 117, 107 859.
- [17] S. Bardiya, J. Jerald, V. Satheeshkumar, *Mater. Sci. Manuf.* **2021**, 39, 1362.
- [18] J. T. Melo, L. Santana, H. T. Idogava, A. I. L. Pais, J. L. Alves, *Eng. Manuf. Lett.* **2022**, 1, 20.
- [19] R. V. Morgan, R. S. Reid, A. M. Baker, B. Lucero, J. D. Bernardin, *Tech. Rep.* **2017**. <https://doi.org/10.2172/1341825>
- [20] D. Anguita, L. Ghelardoni, A. Ghio, L. Oneto, S. Ridella, *ESANN 2012 Proceedings, 20th European Symposium on Artificial Neural Networks, Computational Intelligence and Machine Learning*, ESANN, Belgium **2012**, p. 441.
- [21] L. Buitinck, G. Louppe, M. Blondel, F. Pedregosa, A. Müller, O. Griesel, V. Niculae, P. Prettenhofer, A. Gramfort, J. Grobler, R. Layton, J. Vanderplas, A. Joly, B. Holt, G. Varoquaux, *ECML PKDD Workshop: Languages for Data Mining and Machine Learning*, arXiv, New York **2013**, 108. <https://doi.org/10.48550/arXiv.1309.0238>
- [22] F. Pedregosa, G. Varoquaux, A. Gramfort, V. Michel, B. Thirion, O. Grisel, M. Blondel, P. Prettenhofer, R. Weiss, V. Dubourg, J. Vanderplas, A. Passos, D. Cournapeau, M. Brucher, M. Perrot, E. Duchesnay, *J. Mach. Learn. Res.* **2011**, 12, 2825.
- [23] X. Yan, X. G. Su, *Linear Regression Analysis*, World Scientific, Singapore **2009**, 9. <https://doi.org/10.1142/6986>
- [24] Y. LeCun, Y. Bengio, G. Hinton, *Nature* **2015**, 521, 436.
- [25] A. J. Smola, B. Schölkopf, *Statist. Comput.* **2004**, 14, 199.
- [26] L. Breiman, *Mach. Learn.* **2001**, 45, 5.
- [27] N. S. Altman, *Am. Statist.* **1992**, 46, 175.

## SUPPORTING INFORMATION

Additional supporting information can be found online in the Supporting Information section at the end of this article.

**How to cite this article:** N. Bauriedel, R. Q. Albuquerque, J. Utz, N. Geis, H. Ruckdäschel, *J. Polym. Sci.* **2024**, 62(24), 5633. <https://doi.org/10.1002/pol.20240586>